Pole-Transition Control of Variable-Pole Machines Using Harmonic-Plane Decomposition

Yixuan Wu, *Student Member, IEEE*, Gustaf Falk Olson, *Student Member, IEEE*, and Luca Peretti, *Member, IEEE*

***Abstract*—Variable phase-pole machines have the potential to extend the operational range to higher speeds through magnetic pole changes. The state-of-the-art vector-space decomposition cannot model the transient behavior of the pole change for any possible phase-pole configuration as it creates a discontinuity. The proposed harmonic-plane decomposition theory solves this issue by generalizing the vector-space decomposition to the fullest extend by using its discrete Fourier transformation interpretation. The theory for indirect rotor field-oriented control is developed using the harmonic-plane decomposition. A controlled, loaded pole change on a wound independently-controlled stator-coils machine using two transition strategies shows the harmonic-plane decomposition-based controller's ability to maintain torque in the transition. Additionally, the proposed controller accomplishes real harmonic injection and balanced steady-state operation.**

***Index Terms*—DFT, field oriented control, harmonic plane decomposition, multiphase electric machines, pole change, variable phase-pole machine**

NOMENCLATURE

Subscripts

$\hat{x}$	estimated quantity
x_σ	leakage
x_h	harmonic plane
x_M	magnetizing
x_R	rotor quantity in Γ^{-1}-model
x_r	rotor
x_s	stator
x_{123}	123 fundamental reference frame
$x_{\alpha\beta 0}$	stationary $\alpha\beta 0$ reference frame
x_{dq0}	rotary $dq0$ reference frame
x_{sl}	slip

Variables

α_l	bandwidth of low-pass filter for the MCVM
$\bar{X}_{[.]}$	complex notation of space vector $\mathbf{x}_{[.]}$
δ	spatial phase shift between magnetic axes
$\gamma_{[.]}$	phase shift of a space vector
$\lambda_{[.]}$	modified current model tuning parameter
$\mathbf{C}_{[.]}$	core matrix of Clarke transformation
$\mathbf{T}_{*\mapsto\circ}$	Transformation matrix from $*$ to $\circ$ reference frame
$\mathbf{x}_{[.]}$	real valued vector of $x_{[.]}$
ν	time harmonics order and sequence
$\omega_{[.]}$	rotational frequency
$\psi_{[.]}$	flux linkage
$\tau_e, \tau_e^{sat}, \tau_{\text{shaft}}, \tau_l$	electromagnetic, maximum electromagnetic, shaft and load torque
$\tau_{s,0.5\%}$	settling time with a $0.5\ \%$ tolerance band
φ_h	phase shift of the transformation angle for the Park transformation
ϑ	transformation angle in $\mathbf{C}_r$
$f_{[.]}$	electric frequency
f_{sw}	inverter switching frequency
g	air gap length
h	space harmonic order = harmonic plane
K	factor for amplitude or power invariance
$K_{\{p,i\}}$	proportional and integral gain of controller
K_{mw}	factor for machine coil or toroidal coil
$L_{[.],[.]}$	Γ^{-1}-model inductance
L_a	active length
m	number of phases
n_t	turns ratio
$N_{[.]}$	number of turns per slot
n_{mw}	number of minimum windings
p	number of pole pairs
p_{mw}	number of pole-pairs for minimum windings
q	running number
q_s	slots per pole per phase
$Q_{[.]}$	number of slots
$R_{[.],[.]}$	Γ^{-1}-model resistance
$r_{[.]}$	radius
t	time
$v_{[.]}$, $i_{[.]}$	time-domain voltage/current
v_{dc}	pole-to-pole dc-bus voltage
w_{mw}	number of slots in series per minimum winding
$x_{[.]}$	generic signal that may be replaced by a state or input variable

Manuscript received Month xx, 2xxx; revised Month xx, xxxx; accepted Month x, xxxx.

Y. Wu, G. Falk Olson and L. Peretti are with the Division of Electric Power and Energy Systems, KTH Royal Institute of Technology, Stockholm, Sweden (yixuanw@kth.se, gufo@kth.se, lucap@kth.se).

I. INTRODUCTION

Multiphase electrical machines (MPEMs) have gained significant interest in recent times [1]–[4]. A subgroup of MPEMs aims to improve the torque-speed capability, power density, efficiency, and/or fault tolerance by using independently-controlled stator coils, targeting electric propulsion applications [5]. These have ensued from the development of s.c.

dynamic machine-operation machines [6], conventional variable phase-pole machines (VPPMs) with mechanical or electromagnetic switches to reconfigure the stator windings [7], and machines employing pole-phase modulation (PPM) [8], [9] to electrically change the phase-pole configuration (PPC). Notably, a design study of a variable phase-pole induction machine (IM) in [10], shows that the pole-changing capability enables comparable torque densities to a commercial automotive permanent-magnet synchronous machine while operating at higher efficiencies in the high-speed, low-torque region.

An example of a VPPM is the intelligent stator cage drive (ISCAD) with independently-controlled stator bars [11]. To achieve lower currents, the wound independently-controlled stator-coils machine (WICSC machine) replaces the stator bars with solenoidal coils wound around the stator back [12], or similarly in [13]. These machines allow to control the currents in individual stator slots, differently than conventional MPEMs with series-connected (within one phase) stator windings. A key feature is that they can adopt a multitude of PPCs during real-time operation by adjusting the current in the slots. Thereby, the machine functions as an *electric gearbox*, and the electrical operating point can be switched to minimize losses or maximize the torque per ampere in normal operation [12]. In [14], the necessity of an adapted current control for such machine types is emphasized.

A major challenge is to accomplish a smooth and fast transition between PPCs. In [8], PPM is introduced. It combines two sets of transformations and controllers to achieve the reconfiguration. The same idea has been pursued e.g. in [15]. However, PPM limits itself to configurations with single-slot phase belts only. Moreover, the Clarke matrix is not equal among all configurations. Consequently, each configuration requires its own transformation matrix, introducing a discontinuity. An attempt to fixate the dimension of the Clarke matrix is suggested in [16], where the model relies on the conventional vector-space decomposition (VSD) and therefore uses a weighted sum of the different Clarke and parameter matrices. This may be feasible for low numbers of viable PPCs but becomes more complicated as the number grows. Additionally, the selection of weighting factor is arbitrary during a change between configurations.

This paper deals with the modeling and control of VPPMs and proposes an extended VSD common to all feasible PPCs. Thus, the model is independent of the actual PPC and remains fixed. Specific attention is paid to how to perform a pole transition. The method is intended to be applicable to any VPPM, whereas the matter of determining the optimal PPC, as in [12], is not considered. To motivate, develop and prove the theory, this paper is organized as follows. Section II derives the harmonic-plane decomposition (HPD) as an extension of the VSD through its discrete Fourier transformation (DFT) interpretation. It showcases the analogy between HPD and VSD before presenting an Γ^{-1} model of a multiphase IM. Section III presents a cascaded speed-current controller with a synchronous reference-frame indirect rotor field-oriented control (IFOC) scheme adapted to the HPD theory. In Section IV, a loaded phase-pole transition from a $[m = 9, p = 1]$ to a $[m = 4.5, p = 4]$ PPC is carried out on an experimental test bench. The experiment is conducted on the WICSC machine described in [13]. It validates the proposed HPD controller before Section V concludes the article.

The presented HPD is a generalization of the theory from previous conference papers [17], [18], and provides more insights and experimental support. Notably, a complete equivalent of MPEMs comprising all harmonic planes and independent of PPC is established. The HPD current control strategy is a new addition that adds practical value and addresses the important challenge of ordered pole changes in VPPMs.

II. Harmonic Plane Decomposition

In this work, the HPD theory from [17], [18] provides the foundation for the modeling of a generic VPPM. In contrast to the state-of-the-art VSD, the HPD creates one unified model for all possible PPCs of a VPPM by considering all independent minimum windings of the stator. Opposite to the VSD, the HPD does not require half-wave symmetry of the stator currents. The magnetic axes are considered according to their physical location around the stator circumference in the fundamental 123 reference-frame [19]. This leads to a reorganization of the magnetic axes in the practical abc reference-frame. (1) shows the stator Clarke-transformation in the HPD theory for n_{mw} independently excitable windings, e.g. by n_{mw} inverter legs.

$$\mathbf{x}_{\alpha\beta0} = \underbrace{\left(\frac{2}{n_{mw}}\right)^{K}\mathbf{C}_s}_{\mathbf{T}_{123\to\alpha\beta0}}\cdot\mathbf{x}_{123} \quad \mathbf{x}_{123} = \underbrace{\left(\frac{2}{n_{mw}}\right)^{1-K}\mathbf{C}_s^{\mathrm{T}}}_{\mathbf{T}_{\alpha\beta0\to123}}\cdot\mathbf{x}_{\alpha\beta0}$$

$$\mathbf{C}_s = \begin{bmatrix} 1 & \cos(1\delta) & \cos(2\delta) & \dots & \cos((n_{mw}-1)\delta) \\ 0 & \sin(1\delta) & \sin(2\delta) & \dots & \sin((n_{mw}-1)\delta) \\ 1 & \cos(2\delta) & \cos(4\delta) & \dots & \cos((n_{mw}-1)2\delta) \\ 0 & \sin(2\delta) & \sin(4\delta) & \dots & \sin((n_{mw}-1)2\delta) \\ \vdots & \vdots & \vdots & \ddots & \vdots \\ 1 & \cos(\frac{n_{mw}}{2}\delta) & \cos(2\frac{n_{mw}}{2}\delta) & \dots & \cos((n_{mw}-1)\frac{n_{mw}}{2}\delta) \\ 0 & \sin(\frac{n_{mw}}{2}\delta) & \sin(2\frac{n_{mw}}{2}\delta) & \dots & \sin((n_{mw}-1)\frac{n_{mw}}{2}\delta) \end{bmatrix} \quad \delta = \pi/K_{mw}n_{mw} \tag{1}$$

The magnetic axes in the 123 reference-frame are displaced by the pitch angle δ around the stator circumference. K is a scaling factor for either power- or amplitude-invariance, which is used henceforth. Here, $K_{mw} = 1$ indicates machine coils and $K_{mw} = 0.5$ toroidal windings, respectively. We stress that (1) combines the two bases cases in [17], [18] into one transformation. Further, [17] shows that the Clarke matrix is equal to a complex DFT in space domain, where n_{mw} equals the number of samples in the DFT. Thus, each harmonic plane, h, describes one physical space harmonic in the machine. This becomes more evident when looking at the complex space-vector notation for one harmonic plane in (2).

$$\underbrace{X_{\alpha\beta0,h}e^{j(\nu(h)2\pi f_s t+\gamma_h)}}_{\bar{X}_{\alpha\beta0,h}(t)} = \frac{2}{n_{mw}}\sum_{k=0}^{n_{mw}-1} x_{k+1}(t)e^{jhk\delta} \tag{2}$$

Here, $X_{\alpha\beta0,h}$ is the amplitude and γ_h is the phase of the complex Fourier coefficient in the harmonic plane h. As the base functions of the DFT are orthogonal, the harmonic planes h are also orthogonal, i.e., independent of each other. (3) maps time-harmonic orders, ν, into space harmonics, h, and vice versa. ν has both a sign to indicate the sequence, as well as

an integer value to describe the ordinal of the time harmonic. ν corresponds to a VSD vector space, whereas h represents a HPD harmonic plane. [20, (12)] reports the same mapping in a different context.

$$\nu(h) = \begin{cases} \frac{p_{mw}}{p}h & \text{if } \frac{p_{mw}}{p}h \leq m \\ \frac{p_{mw}}{p}h - 2m & \text{if } m < \frac{p_{mw}}{p}h \leq 3m \\ \frac{p_{mw}}{p}h - 4m & \text{if } 3m < \frac{p_{mw}}{p}h \leq 5m \\ \vdots & \text{if} \quad \vdots \end{cases} \quad \nu(h) \in \mathbb{Z} \tag{3a}$$

$$h(\nu) = (\nu \pm mq)\,\frac{p}{p_{mw}}, \quad \forall \quad \begin{cases} \nu \in \{1, 3, \dots, m\} \\ q \in \{0, 2, 4, \dots\} \end{cases} \tag{3b}$$

In contrast to the modeling of conventional three-phase machines, the HPD needs to cope with cases where there are more independent minimum windings on the stator than the rotor side. For example, the WICSC machine in [13] has $n_{mw} = Q_s = 36$ stator windings and $Q_r = 28$ rotor bars. Thus, the rotor side resolves less space-harmonics by virtue of the Nyquist-Shannon theorem. In order to avoid aliasing, while retaining the dimension of the stator-side reference model, the rotor-side Clarke transformation is adapted to (4).

$$\mathbf{C}_r = \begin{bmatrix} 1 & \cos(1\vartheta) & \dots & \cos((Q_r-1)\vartheta) \\ 0 & \sin(1\vartheta) & \dots & \sin((Q_r-1)\vartheta) \\ \vdots & \vdots & \ddots & \vdots \\ 1 & \cos(\frac{Q_r}{2p_{mw}}\vartheta) & \dots & \cos((Q_r-1)\frac{Q_r}{2p_{mw}}\vartheta) \\ 0 & \sin(\frac{Q_r}{2p_{mw}}\vartheta) & \dots & \sin((Q_r-1)\frac{Q_r}{2p_{mw}}\vartheta) \\ \hline 0 & 0 & \dots & 0 \\ \vdots & \vdots & \ddots & \vdots \\ 0 & 0 & \dots & 0 \end{bmatrix} \begin{matrix} \\ \\ \\ \\ \\ h \leq \left\lfloor \frac{Q_r}{(2p_{mw})} \right\rfloor \\ \hline \\ h > \left\lfloor \frac{Q_r}{(2p_{mw})} \right\rfloor \\ \\ \end{matrix} \tag{4}$$

$$\vartheta = \delta + \theta_r, \quad \delta = \frac{2\pi}{Q_r}, \quad \theta_r(t) = \int_{t_0}^{t} \omega_m(t')dt' + \theta_r(t_0)$$

Finally, the Clarke transformation for rotor quantities is completed in (5) by taking the transformer ratio into account.

$$\begin{aligned} \mathbf{x}_{\alpha\beta 0} &= n_t \cdot \underbrace{\left(2/Q_r\right)^K \mathbf{C}_r}_{\mathbf{T}_{123r\to\alpha\beta 0}} \cdot \mathbf{x}_{123r} \\ \mathbf{x}_{123r} &= 1/n_t \cdot \underbrace{\left(2/Q_r\right)^{1-K} \mathbf{C}_r^{\mathrm{T}}}_{\mathbf{T}_{\alpha\beta 0\to 123r}} \cdot \mathbf{x}_{\alpha\beta 0} \\ n_t &= \begin{cases} \left(N_s/N_r\right)^2 Q_s/Q_r, & v_{[.]}, \psi_{[.]} \\ \left(N_r/N_s\right)^2 Q_r/Q_s, & i_{[.]} \end{cases} \end{aligned} \tag{5}$$

A. Extended Park Transformation Matrix

(1) and (4) establish the space vectors in the stationary $\alpha\beta 0$ reference-frame. A generalized Park transformation brings these into a rotational $dq0$ reference-frame to enable synchronous reference-frame control. Leveraging the independence of the harmonic planes allows to apply a rotation transformation to each of the space vectors separately. The resulting Park transformation matrix in (6) is a block diagonal matrix with 2×2 blocks.

$$\mathbf{T}_{\alpha\beta 0\to dq0} = \begin{bmatrix} a_{1,1} & \dots & a_{1,Q_s} \\ \vdots & \ddots & \vdots \\ a_{Q_s,1} & \dots & a_{Q_s,Q_s} \end{bmatrix} \tag{6}$$

$$\left.\begin{aligned} a_{h,h} &= a_{h+1,h+1} = \cos(2\pi\nu(h)f_s t - \varphi_h) \\ a_{h,h+1} &= -a_{h+1,h} = \sin(2\pi\nu(h)f_s t - \varphi_h) \end{aligned}\right\} \forall\, h, \text{else } 0$$

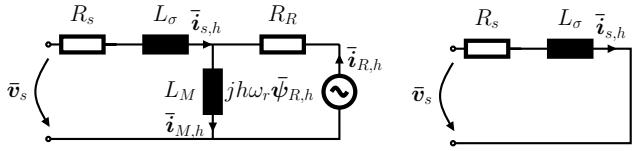

(a) Stator and rotor. (b) Stator only.

Fig. 1: inverse-Γ circuits (a) with rotor and (b) without rotor in harmonic planes h in a stator-oriented reference frame.

According to (3), the space vectors host time harmonics $\nu(h)$ of different orders and sequences depending on the PPC. Consequently, the $dq0$ reference frame must rotate according to the sign and ordinal of $\nu(h)$. Moreover, a phase φ_h allows to shift the harmonic planes relative to each other providing another degree of freedom, which will be used for real harmonic injection (RHI) in Section III-B.

B. Full Model Equations

Having established $\mathbf{C}_s$ and $\mathbf{C}_r$, equivalent-model circuits are deduced. Since the HPD shares the mathematical roots as the VSD, the same assumptions apply, especially magnetic linearity. Assuming that interplane cross-saturation can be neglected [21], i.e. the harmonic planes are independent and each one resembles a three-phase IM. Therefore, we choose to use the Γ^{-1}-model in (7) and depicted in Fig. 1a [22].

$$\begin{aligned} \mathrm{d}\bar{\boldsymbol{\psi}}_{s,\alpha\beta 0,h}/\mathrm{d}t &= \bar{\boldsymbol{v}}_{s,\alpha\beta 0,h} - R_{s,h}\bar{\boldsymbol{i}}_{s,\alpha\beta 0,h} \\ \mathrm{d}\bar{\boldsymbol{\psi}}_{R,\alpha\beta 0,h}/\mathrm{d}t &= jh\omega_r\bar{\boldsymbol{\psi}}_{R,\alpha\beta 0,h} - R_{R,h}\bar{\boldsymbol{i}}_{R,\alpha\beta 0,h} \\ \bar{\boldsymbol{\psi}}_{s,\alpha\beta 0,h} &= L_{M,h}\bar{\boldsymbol{i}}_{M,\alpha\beta 0,h} + L_{\sigma,h}\bar{\boldsymbol{i}}_{s,\alpha\beta 0,h} \\ \bar{\boldsymbol{\psi}}_{R,\alpha\beta 0,h} &= L_{M,h}\bar{\boldsymbol{i}}_{M,\alpha\beta 0,h} \\ \bar{\boldsymbol{i}}_{M,\alpha\beta 0,h} &= \bar{\boldsymbol{i}}_{s,\alpha\beta 0,h} + \bar{\boldsymbol{i}}_{R,\alpha\beta 0,h} \end{aligned} \tag{7}$$

For $h > \left\lfloor Q_r/(2p_{mw}) \right\rfloor$, aliasing of the rotor quantities, as explained in Section II, reduces the model to (8). The equivalent circuit is drawn in Fig. 1b.

$$\mathrm{d}\left[(L_{M,h}+L_{\sigma,h})\bar{\boldsymbol{i}}_{s,\alpha\beta 0,h}\right]/\mathrm{d}t = \bar{\boldsymbol{v}}_{s,\alpha\beta 0,h} - R_{s,h}\bar{\boldsymbol{i}}_{s,\alpha\beta 0,h} \tag{8}$$

Finally, the torque equation of VPPMs in HPD is given in (9).

$$\tau_e = \frac{n_{mw}}{2p_{mw}} K_{mw} \sum\nolimits_h h\bar{\psi}_{R,\alpha\beta 0,h} \times \bar{i}_{s,\alpha\beta 0,h} \tag{9}$$

An example of how to identify the HPD parameters by means of finite-element methods is demonstrated in [23], although it uses the base cases in [17], [18]. An experimental parameter-estimation method for VPPMs is reported in [24].

III. Harmonic Plane Decomposition based Controller

This section proposes a speed-sensored cascaded controller for VPPMs based on the HPD theory. Fig. 2 depicts the controller structure and the following subsections will elaborate on the details of the proposed control.

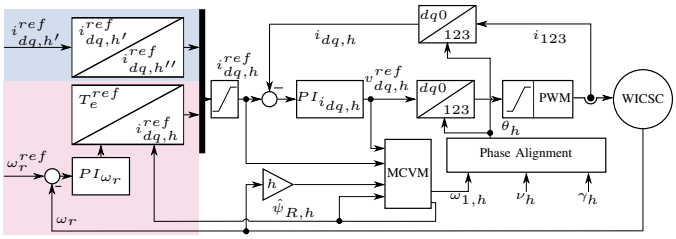

Fig. 2: Full speed and current controller structure. The pink area is valid for a harmonic plane containing the fundamental time harmonic, the blue area is valid for injected harmonics.

A. Current Controller Structure

Section II shows that the HPD performs a DFT on the space-vector quantities, i.e. the space vectors in the $\alpha\beta0$-frame are complex Fourier coefficients of the spatial distribution of the quantity scaled with the appropriate magnitude. Consequently, the harmonic planes are decoupled from one another giving the possibility to control each of them independently. Each harmonic plane can therefore exploit synchronous frame controllers as in a conventional IM. Depending on the PPC, time-harmonics map into different harmonic planes according to (3), which stipulates which harmonic planes to excite. In turn, (2) determines the ratios of the current references.

IFOC is implemented using the modified current-voltage model (MCVM) [22]. The MCVM merges the current model (CM) with a phase-locked loop (PLL). This lowers the sensitivity to errors in the rotor time constant, particularly at higher speeds, which makes the field orientation robust [22]. Using adequate PLL parameters, the field orientation is asymptotically stable [22]. The MCVM is a dynamically weighted combination of the CM and voltage model (VM), favoring the CM at low and the VM at high speeds. (10) reports the rotor flux and slip estimation for each harmonic plane. The rotor flux is aligned with the d-axis in the synchronous reference frame, so that $\bar{\psi}_R = \psi_R$ is real.

$$\begin{aligned}\frac{\mathrm{d}\hat{\psi}_{R,h}}{\mathrm{d}t} &= \hat{R}_{R,h} i^{ref}_{d,h} - \frac{\hat{R}_{R,h}}{\hat{L}_{M,h}}\hat{\psi}_{R,h}\\ \frac{1}{\alpha_l}\frac{\mathrm{d}\omega_{s,h}}{\mathrm{d}t} &= hp_b\omega_r + \frac{\hat{R}_{R,h} i^{ref}_{q,h}}{\hat{\psi}_{R,h}} - k_{pp}\hat{E}_{d,h} - \omega_{s,h}\\ \hat{E}_{d,h} &= v^{ref}_{d,h} - \hat{R}_{s,h} i^{ref}_{d,h} + \omega_{s,h}\hat{L}_{\sigma,h} i^{ref}_{q,h}\end{aligned} \tag{10}$$

For proper weighting, k_{pp} is dynamically updated as (11), which serves as an approximation of [22][(6)].

$$k_{pp} = \lambda_1 \arctan\left(\lambda_2 h\omega_r\right) \tag{11}$$

A PI-controller with cross-coupling cancellation and feed-forward computes the voltage references as in (12).

$$\begin{aligned} e_{d,h} &= i^{ref}_{d,h} - i_{d,h} \qquad e_{q,h} = i^{ref}_{q,h} - i_{q,h}\\ v^{ref}_{d,h} &= K_{p,h} e_{d,h} + K_{i,h}\int e_{d,h}\,\mathrm{d}t - \omega_{s,h} L_{\sigma,h} i^{ref}_{q,h}\\ v^{ref}_{q,h} &= K_{p,h} e_{q,h} + K_{i,h}\int e_{q,h}\,\mathrm{d}t + \omega_{s,h} L_{\sigma,h} i^{ref}_{d,h} + hp_b\omega_r\hat{\psi}_{R,h}\end{aligned} \tag{12}$$

B. Real Harmonic Injection

As the HPD theory describes all excitable space harmonics along the air gap of a VPPM, one can deliberately create non-sinusoidal current, voltage, and air-gap flux linkage waveforms by RHI. This is different to zero-sequence injection, which targets to better utilize the dc-bus voltage. RHI for minimizing a waveform's amplitude has two requirements.

1) All injected frequencies must strictly be integer multiples of one another. Otherwise, there is slip between the frequencies, i.e. the resulting waveform is not stable.
2) The phase between the injected frequencies must be controlled.

(13) follows from requirement 1) by fixating the ratio q between two harmonic planes h', h'', where $h' < h''$. Here, h' contains the fundamental and h'' contains the injected harmonic. For space-harmonic injection, q is a function of h' and h''. In contrast, for time-harmonic injection, q is a function of the mapped time harmonic $v(h)$ determined by the *vector-space distribution* in (3a) for the desired PPC. In case q is not integer, a harmonic injection with this combination of harmonic planes h', h'' is not suited.

$$\left.\begin{aligned}\omega_{s,h'} &= q\omega_{s,h''}\\ \omega_{sl,h'} &= q\omega_{sl,h''}\end{aligned}\right\} \text{where} \begin{cases} q = \frac{\nu(h'')}{\nu(h')} \in \mathbb{N} & \text{time domain}\\ q = \frac{h''}{h'} \in \mathbb{N} & \text{space domain}\end{cases} \tag{13}$$

However, (13) limits the degrees of freedom in control as it couples harmonic plane h' to h'' to ensure the waveform. Consequently, the IFOC from (10) applies only to one harmonic plane, e.g. h', whereas the slip $\omega_{sl,h''}$ becomes dependent. For the sake of control, only one current, e.g. $i_{d,h''}$, remain independent while $i_{q,h''}$ must be calculated from $\omega_{sl,h''}$. Inserting (13) into the generic slip relation (14a) yields (14b) for the injected harmonic planes.

$$\omega_{sl,h} = \hat{R}_{R,h} i^{ref}_{q,h} / \hat{\psi}_{R,h} \tag{14a}$$

$$i_{q,h''} = q \cdot \omega_{sl,h'} \cdot \hat{\psi}_{R,h''} / \hat{R}_{R,h''} \tag{14b}$$

Requirement 2) can be fulfilled by setting the phase angle φ_h in (6) for harmonic planes h' and h''. Depending on the space vector quantity for which the RHI takes place, φ_h must be chosen appropriately. One example is to use RHI to achieve a PPC with $q_s \geq 1$. This is a RHI in current and is achieved by setting $\varphi_h = \gamma_h$ for h' and h'' in (6).

C. Speed Controller

A PI-controller regulates the rotational speed of the WICSC machine. This controller forms an outer feedback loop and supplies the inner current loop with a q-current reference. (15) describes the mechanical behavior of the drive shaft.

$$J\mathrm{d}\omega_r/\mathrm{d}t = b_f\omega_r + \tau_e - \tau_l \tag{15}$$

(16) shows the speed controller with torque anti-windup alongside two calculations from torque reference, τ^{ref}_e, to q-current reference, $i^{ref}_{q,h=p}$. (16)(i) accounts for the flux dynamics while the denominator in (16)(ii) is guaranteed to remain non-zero.

$$\begin{aligned}\tau^{ref}_e &= K_{p,\omega}(\omega^{ref}_r - \omega_r) + K_{i,\omega} I_\omega\\ \mathrm{d}I_\omega/\mathrm{d}t &= \left(\tau^{sat}_e - \tau^{ref}_e\right)/K_{p,\omega} + \omega^{ref}_r - \omega_r\\ i^{ref}_{q,h=p} &= \frac{2\tau^{ref}_e}{n_{mw}p}\begin{cases}\left(\hat{\psi}_{R,h=p}\right)^{-1} & \text{(i)}\\ \left(L_{M,h} i^{ref}_{d,h}\right)^{-1} & \text{(ii)}\end{cases}\end{aligned} \tag{16}$$

D. Pole Transition

One major challenge for the control of a VPPM is how to manage a pole transition. During such a transition, the rotor flux needs to be decreased to zero in the harmonic planes corresponding to the initial configuration, while it is increased to an appropriate level in the harmonic planes corresponding to the desired new configuration. Due to different rotor time constants in the first and second PPC, the (de-)magnetization of the two harmonic planes take differently long time. Some possible implications during a transition encompass interplane cross-saturation [21], torque loss and overcurrents.

The proposed HPD provides the modeling foundation for controlling such a pole transition seamlessly without discontinuities. A *hard switch* of torque production from $h^{(1)}$ to $h^{(2)}$ without any special pole-transition control shows the capability of the modeling approach in isolation. Fig. 3a shows the ideal currents $i_{dq,h^{(1)}}$ and $i_{dq,h^{(2)}}$ of such a pole transition.

Here, $h^{(1)} = p^{(1)}$ is demagnetized at the same time as $h^{(2)} = p^{(2)}$ is magnetized. Simultaneously, the torque production switches to the new configuration by means of (16). At the pole transition, $\psi_{R,h^{(2)}} = 0$. To maintain the torque, $i_{q,h^{(2)}} \to \infty$ is required. Using (16)(ii) when converting τ_e^{ref} to $i_{q,h^{(2)}}^{ref}$ avoids a division by zero at the pole transition instance but it overestimates the $\psi_{R,h^{(2)}}$, which leads to a longer transient. In this case, a torque loss is inevitable. The torque recovery is limited by the flux linkage dynamics in $h^{(2)}$.

On the one hand, it is desirable to excite $i_{d,h^{(2)}}$ prior to the actual pole transition to fully magnetize $h^{(2)}$ for a smaller torque dip. On the other hand, this is not reasonable because it requires that $h^{(1)}$ is fully demagnetized in order to avoid magnetic saturation, which leads to $i_{q,h^{(1)}} \to \infty$ for a constant torque. A compromise between peak current, magnetization and recovery time is struck by overlapping the two flux linkages $\psi_{R,h^{(1)}}$ and $\psi_{R,h^{(2)}}$. Fig. 3b illustrates this strategy. The three time instances are: 1) Predemagnetization, 2) Premagnetization, 3) Pole Transition. A non-zero $\psi_{R,h^{(2)}}$ warrants (16)(i) when computing $i_{q,h^{(2)}}^{ref}$.

IV. Experimental Results

In this section, a $4.5\,\mathrm{Nm}$ loaded pole transition from $[m = 9, p = 1]$ to $[m = 4.5, p = 4]$ is carried out and analyzed to validate the HPD theory and to assess the control scheme. The chosen PPCs demonstrate the ability of the HPD to model configurations with different q_s, p odd and even, and m integer and non-integer. It also avoids radial forces on the bearings, which occur when $|\,h^{(1)} - h^{(2)}| = 1$ [8].

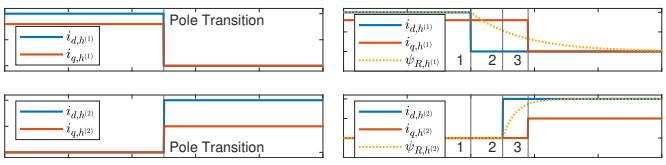

(a) Hard switch (b) Premagnetized switch

Fig. 3: Idealized currents and rotor flux linkages $i_{dq,h^{(1)}}$, $\psi_{R,h^{(1)}}$, and $i_{dq,h^{(2)}}$, $\psi_{R,h^{(2)}}$ before and after the pole switch.

Q_s	Q_r	P_n [kW]	ω_n [rpm]	I_n [A]	V_n [V]	$\cos\phi$	τ_n [Nm]	$f_{50s,n}$ [Hz]
36	28	15	2934	15.1	690	0.9	48.8	50

PI_ω		$\mathrm{PI}_{i_{dq}}$						MCVM	
$K_{p,\omega}$	$K_{i,\omega}$	$K_{p,1}$	$K_{i,1}$	$K_{p,4}$	$K_{i,4}$	$K_{p,17}$	$K_{i,17}$	λ_1	λ_2
3	7.5	17.5	1000	16.5	888	5	100	$2/\pi$	0.2

TABLE I: Original machine *3GAA161420-BDG* [25] nominal operation and control tuning parameters.

A. Experimental Setup

Fig. 4 schematically depicts the terminal connections of the WICSC machine. It consists of a $n_{mw} = Q_s$-leg, two-level voltage-source inverter supplied from a DC-bus voltage of $v_{dc} = 107\,\mathrm{V}$. The outputs of the inverter connect to the WICSC machine with minimum windings of $w_{mw} = 1$. Thus, $K_{mw} = 0.5$. The other end of these windings form one single isolated neutral point. Notice that each stator-slot is individually excited and the current controller needs to excite the toroids appropriately to form a balanced set of m-phase, $2p$-pole currents. The current in each minimum winding is measured with a current transducer. An encoder is mounted on the shaft of the WICSC machine to measure the speed, whereas a torque transducer is mounted between the shaft of the WICSC machine and the shaft of the load machine, as depicted in Fig. 5. The inverter implements carrier-based sinusoidal pulse width modulation with $f_{sw} = 8\,\mathrm{kHz}$, and symmetric, regular reference sampling as modulation scheme.

Table I shows the nominal values of the original three-phase machine, whereas [13] contains the details about the WICSC machine conception along with controller parameters for the harmonic planes containing the fundamental time harmonic. Controllers are also present in all other harmonic planes to force the currents in these to zero. The electrical parameters are and summarized in Table II [24]. In the

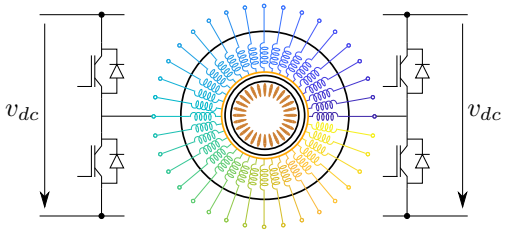

Fig. 4: Schematic of the WICSC machine with Q_s independent stator coils (color shade) and Q_r rotor bars (brown). Only two inverter legs are shown for clarity.

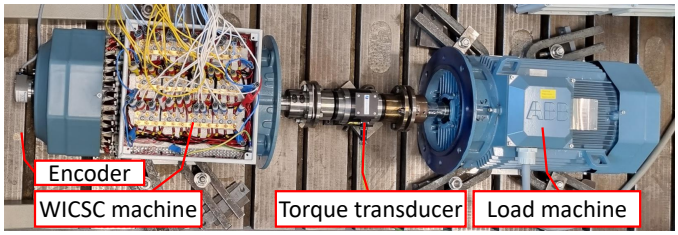

Fig. 5: WICSC machine with load machine.

h	R_s	L_σ	L_M	R_R	h	R_s	L_σ	L_M	R_R
1	318	5.6	155	203	10	318	3.5	3.2	53
2	318	4.5	38.2	126	11	318	3.5	3.2	53
3	318	4.2	16.5	101	12	318	3.5	3.2	53
4	318	3.9	8.7	82	13	318	3.5	3.2	53
5	318	3.8	5.4	68	14	318	3.5	3.2	53
6	318	3.5	3.2	53	15	318	6.7	-	-
7	318	3.5	3.2	53	16	318	6.3	-	-
8	318	3.5	3.2	53	17	318	6.0	-	-
9	318	3.5	3.2	53	18	318	5.5	-	-

TABLE II: Electrical parameters of the WICSC machine. Resistances in [mΩ] and inductances in [mH].

experiments, the machine is excited only with the fundamental time harmonic. The $[m = 9, p = 1]$ PPC has $q_s = 2$, so $h = \{1, 17\}$ contain the fundamental and need to be excited, following (3). In other words, a RHI of a 17^{th} space harmonic yields the desired PPC. Applying (2), the stationary reference frame currents are $\bar{I}_{\alpha\beta 0,h=1} = 0.996\hat{i}_{123}e^{-j0.0873}$ and $\bar{I}_{\alpha\beta 0,h=17} = 0.0872\hat{i}_{123}e^{-j1.48}$. Thus, setting $\varphi_{h=1} = 0.0873$ and $\varphi_{h=17} = 1.48$ in (6) implies that two adjacent slots belonging to the same phase belt share identical currents.

According to (4), $h = 17$ does not present any coupling between the stator and the rotor. As a result, this harmonic plane does not produce torque. Therefore, the speed controller from Section III-C only outputs $i^{ref}_{q,h=1}$ for the $[m = 9, p = 1]$ PPC. While scaling the magnitude of $\bar{i}_{dq,h=17}$ appropriately to achieve the desired PPC is important, the decoupling from the rotor allows to divide the d- and q-currents equally as $i^{\text{ref}}_{d,h=17} = i^{\text{ref}}_{q,h=17} = \left|\underline{k}_{d,h=17}/(\sqrt{2}\underline{k}_{d,h=1})\right| |\bar{i}^{\text{ref}}_{dq,h=1}|$.

$h = 4$ is exclusively excited in the $[m = 4.5, p = 4]$ configuration. The non-integer number of phases is a consequence of the relation between the number of independent windings and the number of pole pairs: $m = {}^{n_{mw}}/_{2p} = {}^{Q_s}/_{2\cdot 4} = 4.5$.

The two pole transitions from Fig. 3a and Fig. 3b are presented. In the latter, the times are chosen as $t_{preDeMag} = 0.69\tau_{R,h=1} = 0.528\,\text{s}$ and $t_{preMag} = 2\tau_{R,h=4} = 0.211\,\text{s}$. This results in $\psi_{R,h^{(1)}}(t = 30.0\,\text{s}) \approx 0.5\psi_{R,h^{(1)}}(t_{preDeMag})$ and $\psi_{R,h^{(2)}}(t = 30.0\,\text{s}) \approx 0.865\psi_{R,h^{(2)}}(t \to \infty)$, which should avoid magnetic saturation.

B. Analysis of Experimental Results

The measured steady-state current distributions at an arbitrary time instance for both PPCs are visualized in Fig. 6. The figure highlights that the desired PPCs are accomplished

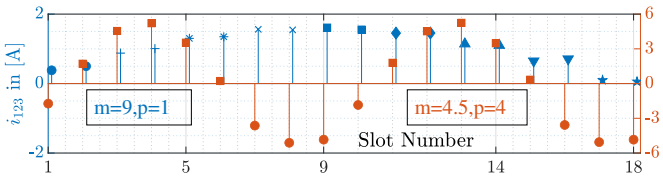

Fig. 6: Current distributions over 180°: $[m = 9, p = 1]$ in blue shows adjacent currents are controlled to be (almost) identical. $[m = 4.5, p = 4]$ in orange has unequal positive (square) and negative (circle) poles, resulting in a non-integer m.

with minor differences between currents belonging to the same phase belt. This can be ascribed to measurement noise and controller imperfections.

Next, Fig. 7 depicts for both the hard and premagnetized transitions $i_{dq,h=\{1,4,17\}}$, slot currents $i_{\{1,10\}}$, and ω_r, together with τ_{shaft}, which is notch filtered to remove mechanical resonances of the laboratory bench. The pole transition as well as the starting instances of the (de-)magnetizations are indicated by vertical lines. A closer look at Fig. 7 reveals several conclusions.

Firstly, the 123-currents in steady state are appropriately aligned. The amplitudes are the same in both minimum windings, i.e. toroids, and the phase displacements correspond to the desired PPCs, namely ${}^{4\pi}/_{9}$ and $0\,\text{rad}$, before and after the transition, respectively. This proves that balanced steady-state operation of the desired current distribution in the slots is achievable using the HPD.

Secondly, the dq-currents follow the references with good agreement, indicating that the decoupled current control is successful using the HPD with associated field alignment.

Thirdly, the pole-transition is conducted orderly, solely by applying the appropriate current references. Despite changing the PPC, the HPD guarantees continuity in the control structure. The number of harmonic planes remains the same, which allows a continuous modeling of the WICSC machine.

Fourthly, comparing Fig. 7a to Fig. 7b shows that the electrical transient after the pole change is compressed by $\approx$100 ms when premagnetizing the rotor flux in $h^{(2)}$ while demagnetizing $h^{(1)}$. Further, in Fig. 7c the speed recovers more quickly to the reference level. The settling time using $0.5\,\%$ tolerance bands around ω_r^{ref}, as indicated by the dashed horizontal lines, is reduced by $64\,\text{ms}$.

Fifthly, Fig. 7b shows that $i^{\text{ref}}_{q,h^{(1)}}$ increases during the de- and premagnetization phases to compensate for the torque reduction caused by the exponential decrease in $\psi_{R,h^{(1)}}$. Despite that, the slot currents remain approximately the same as in the hard switched case. It can be ascribed to the overestimation of $\psi_{R,h^{(2)}}$ in (16)(ii). During the pre-magnetization, the slot currents contain a first and fourth time-harmonic indicating that two magnetic fields of different order are excited concurrently.

The experimental results confirm the behavior anticipated in Section III-D.

V. Conclusion

This paper presented the harmonic-plane decomposition, an extension of the vector-space decomposition for modeling of variable phase-pole machines. By generalizing the discrete Fourier transformation interpretation of the vector-space decomposition, it unifies the transformations for all phase-pole configuration. Experiments showing the steady state of and transition between two phase-pole configurations validated the properties of the harmonic-plane decomposition and the proposed indirect rotor field-oriented control. Finally, two phase-pole transition strategies were compared experimentally. A pre- (de-)magnetization of the magnetic fields for the phase-pole configurations before and after the transition promise to reduce the mechanical transition time. Future work aims to further optimize the electrical and mechanical transients.

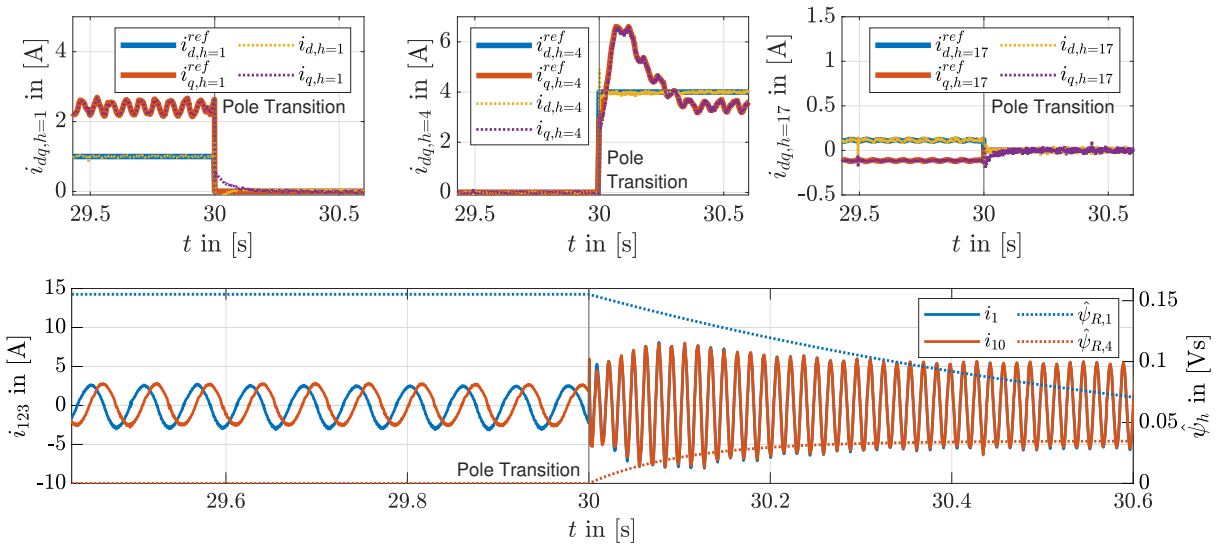

(a) Hard switched transition. Magnetization and torque production change simultaneously from $h = 1$ to $h = 4$. The excitation of $h = 17$ to emulate a $m = 9, p = 1$ configuration stops at the same time. Maximum current amplitude during transition is $\hat{i}_{123} = 8.22\,\mathrm{A}$.

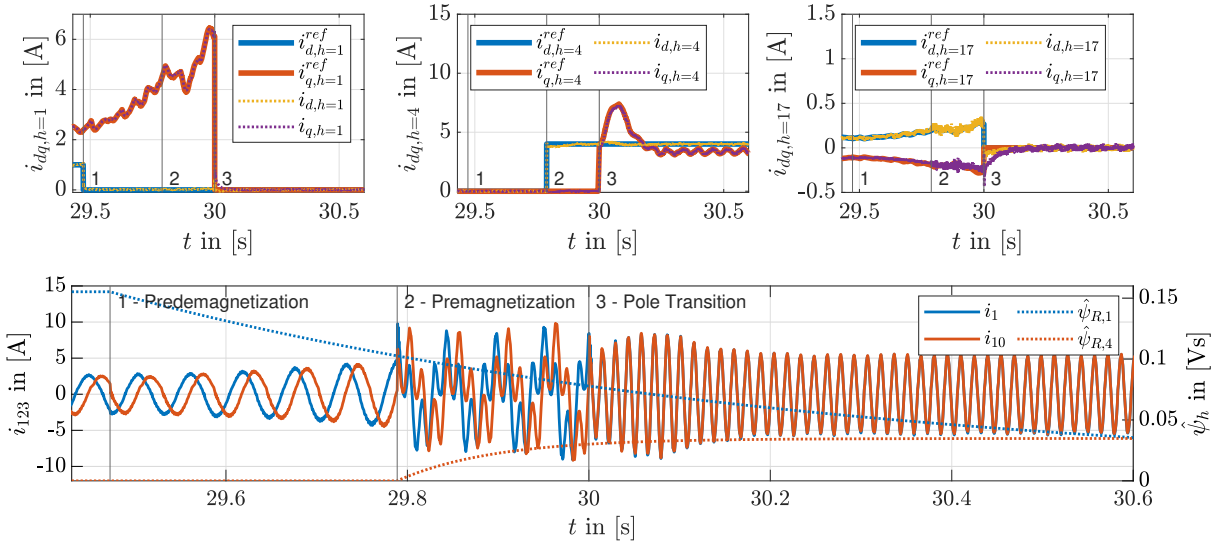

(b) Predemagnetization with $t_{preDeMag} = 0.69\tau_{R,h=1} = 0.528\,\mathrm{s}$ and premagnetization with $t_{preMag} = 2\tau_{R,h=4} = 0.211\,\mathrm{s}$. The two-pole and eight-pole fields ramp down at t_1 and up at t_2, respectively. The torque production is kept in $h = 1$ until t_3, when it transitions to $h = 4$. Concurrently, excitation ceases in $h = 17$. Maximum current amplitude during transition is $\hat{i}_{123} = 10.6\,\mathrm{A}$.

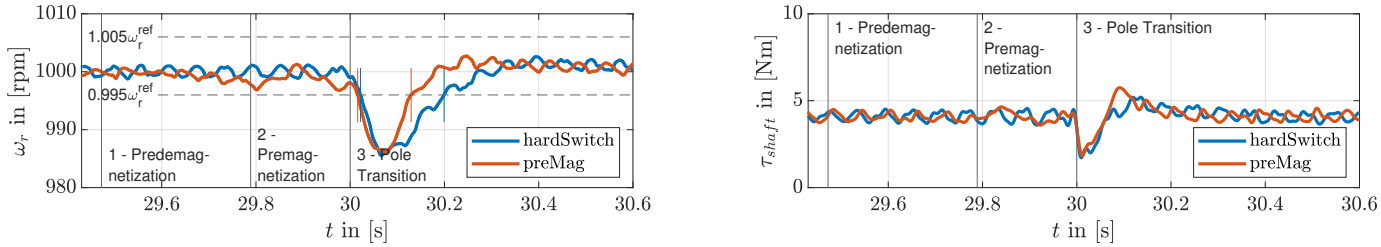

(c) Comparison of ω_r and τ_{shaft} for the hard switch and the premagnetized pole transition. $\tau_{\mathrm{s},0.5\,\%,\mathrm{hardSwitch}} = 0.177\,\mathrm{s}$ and $\tau_{\mathrm{s},0.5\,\%,\mathrm{preMag}} = 0.113\,\mathrm{s}$.

Fig. 7: Rotational $dq0$ reference-frame currents in harmonic planes $h \in \{1, 4, 17\}$, 123 reference-frame currents i_1, i_{10} during the pole transition from $[m = 9, p = 1]$ to $[m = 4.5, p = 4]$ PPC with current and speed control at $\omega_r^{ref} = 1003\,\mathrm{rpm}$.

REFERENCES

[1] E. Levi, R. Bojoi, F. Profumo, H. A. Toliyat, and S. Williamson, "Multiphase induction motor drives - a technology status review," *IET Electric Power Applications*, vol. 1, DOI 10.1049/iet-epa:20060342, no. 4, pp. 489–516, 2007.

[2] F. Barrero and M. J. Duran, "Recent advances in the design, modeling, and control of multiphase machines—part I," *IEEE Transactions on Industrial Electronics*, vol. 63, DOI 10.1109/TIE.2015.2447733, no. 1, pp. 449–458, 2016.

[3] A. Cervone, M. Slunjski, E. Levi, and G. Brando, "Optimal third-harmonic current injection for asymmetrical multiphase permanent magnet synchronous machines," *IEEE Transactions on Industrial Electronics*, vol. 68, DOI 10.1109/TIE.2020.2982099, no. 4, pp. 2772–2783, 2021.

[4] S. Rubino, I. R. Bojoi, F. Mandrile, and E. Armando, "Modular stator flux and torque control of multi-three-phase induction motor drives," *IEEE Transactions on Industry Applications*, vol. 56, DOI 10.1109/TIA.2020.3022338, no. 6, pp. 6507–6525, 2020.

[5] B. Ge, D. Sun, W. Wu, and F. Z. Peng, "Winding design, modeling, and control for pole-phase modulation induction motors," *IEEE Transactions on Magnetics*, vol. 49, DOI 10.1109/TMAG.2012.2208652, no. 2, pp. 898–911, 2013.

[6] T. Gerrits, C. G. E. Wijnands, J. J. H. Paulides, and J. L. Duarte, "Fault-tolerant operation of a fully electric gearbox equivalent," *IEEE Transactions on Industry Applications*, vol. 48, DOI 10.1109/TIA.2012.2222332, no. 6, pp. 1855–1865, 2012.

[7] M. Boxriker, J. Kolb, and M. Doppelbauer, "Effects of coil configuration switching, pole-changing and multi-phase windings on permanent magnet synchronous motors," in *IECON 2017 - 43rd Annual Conference of the IEEE Industrial Electronics Society*, DOI 10.1109/IECON.2017.8216325, Conference Proceedings, pp. 1925–1932.

[8] M. Osama and T. A. Lipo, "Modeling and analysis of a wide-speed-range induction motor drive based on electronic pole changing," *IEEE Transactions on Industry Applications*, vol. 33, DOI 10.1109/28.633794, no. 5, pp. 1177–1184, 1997.

[9] B. Ge, D. Sun, W. Wu, and F. Z. Peng, "Winding design, modeling, and control for pole-phase modulation induction motors," *IEEE Transactions on Magnetics*, vol. 49, DOI 10.1109/TMAG.2012.2208652, no. 2, pp. 898–911, 2013.

[10] Y. Matsuyama, K. Ishizuka, T. Kosaka, H. Matsumori, and N. Matsui, "Design study on high torque density multiphase pole-change induction motor for vehicle propulsion drive," in *2021 24th International Conference on Electrical Machines and Systems (ICEMS)*, DOI 10.23919/ICEMS52562.2021.9634455, pp. 426–431, 2021.

[11] G. Dajaku and D. Gerling, "Low costs and high efficiency asynchronous machine with stator cage winding," in *2014 IEEE International Electric Vehicle Conference (IEVC)*, DOI 10.1109/IEVC.2014.7056083, Conference Proceedings, pp. 1–6.

[12] E. Libbos, B. Ku, S. Agrawal, S. Tungare, A. Banerjee, and P. T. Krein, "Loss minimization and maximum torque per ampere operation for variable-pole induction machines," *IEEE Transactions on Transportation Electrification*, DOI 10.1109/TTE.2020.2997692, pp. 1–1, 2020.

[13] K. Bitsi, O. Wallmark, and S. Bosga, "An induction machine with wound independently-controlled stator coils," in *2019 22nd International Conference on Electrical Machines and Systems (ICEMS)*, DOI 10.1109/ICEMS.2019.8921779, Conference Proceedings, pp. 1–5.

[14] S. Runde, A. Baumgardt, O. Moros, B. Rubey, and D. Gerling, "ISCAD — design, control and car integration of a 48 volt high performance drive," *CES Transactions on Electrical Machines and Systems*, vol. 3, DOI 10.30941/CESTEMS.2019.00017, no. 2, pp. 117–123, 2019.

[15] M. P. Magill and P. T. Krein, "A dynamic pole-phase modulation induction machine model," in *2015 IEEE International Electric Machines & Drives Conference (IEMDC)*, DOI 10.1109/IEMDC.2015.7409030, Conference Proceedings, pp. 13–19.

[16] B. P. Reddy, A. Iqbal, S. Rehaman, M. Meraj, and S. Keerthipati, "Dynamic modelling and control of pole-phase modulation based multiphase induction motor drives," *IEEE Journal of Emerging and Selected Topics in Power Electronics*, DOI 10.1109/JESTPE.2021.3062216, pp. 1–1, 2021.

[17] Y. Wu, G. Falk Olson, L. Peretti, and O. Wallmark, "Harmonic plane decomposition: An extension of the vector-space decomposition - part I," in *IECON 2020 - 46th Annual Conference of the IEEE Industrial Electronics Society*, DOI 10.1109/IECON43393.2020.9255228, Conference Proceedings.

[18] G. Falk Olson, Y. Wu, L. Peretti, and O. Wallmark, "Harmonic plane decomposition: An extension of the vector-space decomposition - part II," in *IECON 2020 - 46th Annual Conference of the IEEE Industrial Electronics Society*, DOI 10.1109/IECON43393.2020.9254279, Conference Proceedings.

[19] A. A. Rockhill and T. A. Lipo, "A generalized transformation methodology for polyphase electric machines and networks," in *2015 IEEE International Electric Machines & Drives Conference (IEMDC)*, DOI 10.1109/IEMDC.2015.7409032, Conference Proceedings, pp. 27–34.

[20] S. Williamson and S. Smith, "Pulsating torque and losses in multiphase induction machines," *IEEE Transactions on Industry Applications*, vol. 39, DOI 10.1109/TIA.2003.813722, no. 4, pp. 986–993, 2003.

[21] J. Milos, B. Brkovic, E. Levi, and Z. Lazarevic, "Interplane cross-saturation in multiphase machines," *IET Electric Power Applications*, vol. 13, DOI 10.1049/iet-epa.2018.5546, no. 11, p. 1812 – 1822, 2019.

[22] L. Harnefors, "Design and analysis of general rotor-flux-oriented vector control systems," *IEEE Transactions on Industrial Electronics*, vol. 48, DOI 10.1109/41.915417, no. 2, pp. 383–390, 2001.

[23] Y. Wu, A. Pisani, G. Falk Olson, K. Bitsi, O. Wallmark, and L. Peretti, "FEM-based parameter estimation for a variable phase-pole induction machine," in *The 23rd European Conference on Power Electronics and Applications (EPE 2021)*, Conference Proceedings, 2021. [Online]. Available: https://ieeexplore.ieee.org/document/9570586

[24] G. Falk Olson and L. Peretti, "Parameter estimation of multiphase machines applicable to variable phase-pole machines," in *2022 International Conference on Electrical Machines (ICEM)*, DOI 10.1109/ICEM51905.2022.9910883, Conference Proceedings, pp. 949–955.

[25] ABB. 3gaa161420-bdg. Accessed: 2022-10-31. [Online]. Available: https://new.abb.com/products/sv/3GAA161420-BDG/3gaa161420-bdg

Yixuan Wu received his M.Sc. in electrical engineering from the RWTH Aachen University, Aachen, Germany and KTH Royal Institute of Technology, Stockholm, Sweden in 2019.

Since 2019, he has been a PhD student at the Division for Electrical Power and Energy Systems (EPE) at KTH Royal Institute of Technology, Stockholm, Sweden. His research interests include modeling and control of variable phase-pole drives, power electronics, fault-tolerance and electromobility.

Gustaf Falk Olson was born in Kristinehamn, Sweden. He received the M.Sc. in electrical power engineering from the Royal Institute of Technology KTH, Stockholm, Sweden in 2016.

After graduation he worked as a Field Application Engineer for Texas Instruments. Since 2019, he has been a PhD student at the Division for Electrical Power and Energy Systems (EPE) at KTH Royal Institute of Technology, Stockholm, Sweden. His research interests include modeling, control, and parameter estimation of multiphase machines for vehicle and power generation applications.

Luca Peretti received the M. Sc. degree in Electronic Engineering in 2005 from the University of Udine, Italy, and the Ph.D. degree from the University of Padova, Italy, in 2009. Between November 2007 and March 2008, he was a visiting Ph.D. student at ABB Corporate Research, Västerås, Sweden. From August 2010 to August 2018, he was with ABB Corporate Research, Västerås, Sweden in different roles as principal scientist, project leader and strategy coordinator. He has also been an Affiliated Faculty member at KTH, division of Electric Power and Energy Systems, since July 1, 2016. From September 2018 Luca is an Associate Professor at KTH, division of Electric Power and Energy Systems, in the field of Electric Machines and Drives. His main scientific interests relate to the automatic parameter estimation in electric machines, sensorless control, loss segregation in drive systems, multiphase drives, condition monitoring of machines and drives, in the context of industrial, wind energy and traction applications.